frontiers in Physics

ORIGINAL RESEARCH
published: 24 March 2022
doi: 10.3389/fphy.2022.838524

Electron-Ion Temperature Relaxation in Warm Dense Hydrogen Observed With Picosecond Resolved X-Ray Scattering

L. B. Fletcher[1], J. Vorberger[2], W. Schumaker[1], C. Ruyer[1], S. Goede[1,3], E. Galtier[1], U. Zastrau[3], E. P. Alves[1], S. D. Baalrud[4], R. A. Baggott[5,6], B. Barbrel[7], Z. Chen[1,8], T. Döppner[9], M. Gauthier[1], E. Granados[1], J. B. Kim[1], D. Kraus[7,2], H. J. Lee[1], M. J. MacDonald[1,10], R. Mishra[1], A. Pelka[2], A. Ravasio[11], C. Roedel[1], A. R. Fry[1], R. Redmer[12], F. Fiuza[1], D. O. Gericke[5] and S. H. Glenzer[1]*

[1]SLAC National Accelerator Laboratory, Stanford University, Menlo Park, CA, United States, [2]Helmholtz-Zentrum Dresden-Rossendorf, High Energy Density Physics, Dresden, Germany, [3]European XFEL, Schenefeld, Germany, [4]Department of Physics and Astronomy, University of Iowa, Iowa City, IA, United States, [5]Centre for Fusion, Space and Astrophysics, Department of Physics, University of Warwick, Coventry, United Kingdom, [6]Blackett Laboratory, Imperial College London, London, United Kingdom, [7]Department of Physics, University of California, Berkeley, Berkeley, CA, United States, [8]University of Alberta, Edmonton, AB, Canada, [9]Lawrence Livermore National Laboratory, Livermore, CA, United States, [10]University of Michigan, Ann Arbor, MI, United States, [11]Laboratoire pour L'Utilisation des Lasers Intenses, Palaiseau, France, [12]Universität Rostock, Institut für Physik, Rostock, Germany

Angularly resolved X-ray scattering measurements from fs-laser heated hydrogen have been used to determine the equilibration of electron and ion temperatures in the warm dense matter regime. The relaxation of rapidly heated cryogenic hydrogen is visualized using 5.5 keV X-ray pulses from the Linac Coherent Light (LCLS) source in a 1 Hz repetition rate pump-probe setting. We demonstrate that the electron-ion energy transfer is faster than quasi-classical Landau-Spitzer models that use *ad hoc* cutoffs in the Coulomb logarithm.

Keywords: non-equilibrium plasma, electron-ion equilibration, warm dense hydrogen, x-ray thomson scattering, ultrafast x-ray scattering

OPEN ACCESS

Edited by:
Jiayu Dai,
National University of Defense Technology, China

Reviewed by:
Taras Bryk,
Institute for Condensed Matter Physics, Ukraine
Hao Liu,
Hunan University, China

****Correspondence:***
L. B. Fletcher
lbfletch@slac.stanford.edu

Specialty section:
This article was submitted to Atomic and Molecular Physics, a section of the journal Frontiers in Physics

Received: *17 December 2021*
Accepted: *09 February 2022*
Published: *24 March 2022*

Citation:
Fletcher LB, Vorberger J, Schumaker W, Ruyer C, Goede S, Galtier E, Zastrau U, Alves EP, Baalrud SD, Baggott RA, Barbrel B, Chen Z, Döppner T, Gauthier M, Granados E, Kim JB, Kraus D, Lee HJ, MacDonald MJ, Mishra R, Pelka A, Ravasio A, Roedel C, Fry AR, Redmer R, Fiuza F, Gericke DO and Glenzer SH (2022) Electron-Ion Temperature Relaxation in Warm Dense Hydrogen Observed With Picosecond Resolved X-Ray Scattering. Front. Phys. 10:838524. doi: 10.3389/fphy.2022.838524

1 INTRODUCTION

Understanding the properties of warm dense hydrogen is important for modeling and predicting the energy flow in many short-lived fusion-relevant platforms such as self-constricted plasmas found in Z-pinches [1], as well as for inertial confinement fusion (ICF) experiments [2]. Critical to the mission of inertial fusion is the knowledge of the electron-ion energy transfer and their temperature equilibration times in a high-energy-density state. The complex interplay of collisional and collective processes driving this relaxation also determines transport properties, like the thermal conductivity and stopping power. Thus, precise knowledge of the electron-ion relaxation strongly furthers our ability to accurately model complex systems such as the hot-spot at stagnation and the deuterium-tritium fuel-ablator interface in an ICF implosion [3–5]. Ultrafast X-ray scattering is a premier way to investigate such processes while yielding additional information on the structural and collective properties of dense matter [6–13].

Temperature relaxation in a dense, moderately coupled and partially degenerate plasma is challenging since it requires consideration of quantum degeneracy of the electron subsystem, the ionic short range structure, strong collisions, and coupling effects from the ions [14–18]. The seminal

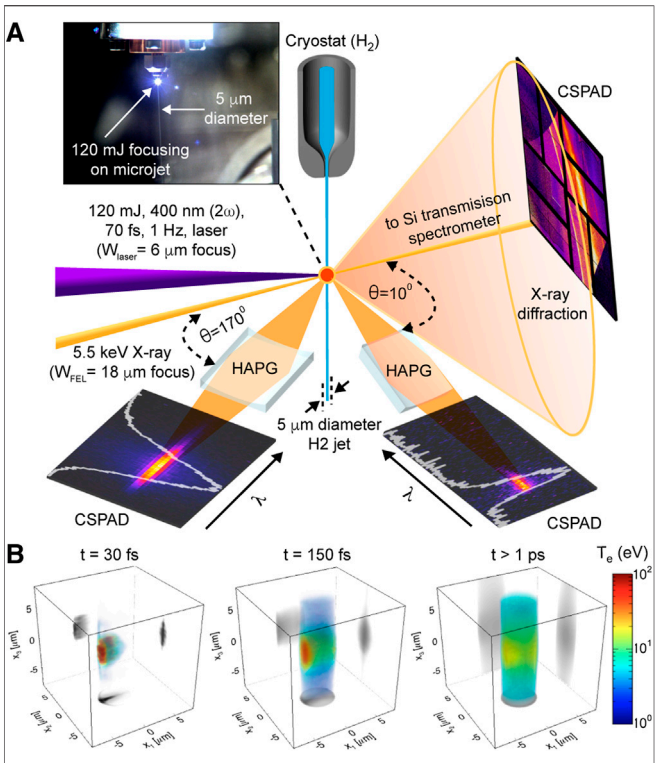

FIGURE 1 | (color online) **(A)** Ultrafast pump-probe schematic of experimental setup showing the LCLS X-ray beam scattering in 1 Hz repetition from a fs-irradiated 5 μm H_2 diameter jet. The scattered photons are captured on a Cornell SLAC Pixel Array Detectors (CSPADs) to angularly resolve the static structure factor as well as measure the changes to the lattice structure over ps time steps. The data overlaid on the backward, k = 4.8 nm^{-1}, crystal spectrometer resolves inelastic scattered X-rays. The data overlaid on the forward, k = 52 nm^{-1}, spectrometer resolves elastically and inelastically scattered X-rays. **(B)** 3D OSIRIS simulations showing time evolution of electron heating induced by the fs-laser; The laser produces a hot electron population with slope temperature of 14.3 keV *via* $J \times B$ heating. At t < 50 fs, the background electrons at the surface are heated to $T_e \gtrsim 100$ eV. At t = 150 fs, fast electrons then recirculate in the target, heating the background through a combination of collisionless and collisional processes; At t ≥ 1 ps, fast electrons thermalize with the background electrons averaged over the experimental scattering volume, $< T_e > \sim 10$ eV, where subsequent electron-ion relaxation and equilibration occur.

Landau-Spitzer approach sufficiently describes contributions from binary collisions in weakly interacting, classical plasmas [19, 20], but it completely fails for denser, or colder, systems where the Coulomb logarithm becomes negative. In order to prevent this unphysical behavior, empirically modified or capped forms for the Coulomb logarithm have been suggested without being rigorously tested against experiments [21–24]. Until now, the electron-ion relaxation in dense plasmas have only been inferred, or extrapolated, indirectly from experimental data [25–27] that is measured under equilibrium conditions. Furthermore, determining the energy exchange from electrons to ions and atoms in dense matter requires the preparation of a homogeneous sample and ultrafast probing. The Matter in Extreme Conditions (MEC) end-station at the LCLS provides a unique platform that can isochorically and uniformly heat hydrogen from a cryogenic state to the warm dense matter regime while providing ultrashort, picosecond delayed X-ray pulses that can be scattered and resolved in both energy and wavenumber.

In this article, we present experimental evidence of picosecond resolved electron-ion energy relaxation in dense non-equilibrium hydrogen plasmas using angularly resolved X-ray Thomson scattering. Our results demonstrate that a uniformly heated hydrogen plasma in the warm dense state, approaching an electron temperature of 10 eV at 1 ps, will continue to equilibrate to a temperature state of T_e=T_i=4.5 eV. The results show an electron-ion thermalization time that is shorter than that calculated using a Spitzer-like approach with a generalized Coulomb logarithm, and agrees well with theories that correct the standard Spitzer result to describe the scattering process quantum mechanically [14, 15, 18, 28, 29]. Such models include electron degeneracy and energy transfer *via* coupled collective modes.

2 EXPERIMENT

Figure 1 shows a schematic of the experimental setup at the MEC end-station of the LCLS. A 70 fs, frequency doubled Ti:sapphire laser system was used to isochorically heat a 5 μm diameter hydrogen jet to a non-equilibrium state. Initially, liquid hydrogen was held in a helium cooled cryostat at temperatures T = 17 K. It was injected into the MEC vacuum chamber, whereby it evaporatively cooled to cryogenic solid H_2. Using a pulse energy of 120 mJ focused to spot size of 6 μm (w_{laser}), vertically polarized along the jet axis, resulted in a peak laser intensity of 5×10^{17} W/cm^2 delivered to the hydrogen jet. Separately, the LCLS X-ray beam at 5.5 keV with a FWHM pulse duration of 62 fs (aligned 45°with respect to the laser axis) was delayed at time steps of 1, 2.5, 5, 10, and 25 ps after the fs-laser pulse, and used to measure the plasma properties by applying spectrally and angularly resolved X-ray scattering. The X-ray pulse energy was 4 mJ (3.8×10^{12} photons per pulse), and was focused using a beryllium lens stack to a focal diameter (w_{FEL}) of approximately 18 μm.

A fixed angle X-ray scattering spectrometer in the collective scattering regime was used in the forward direction, corresponding to a probing wave vector of k = 4.8 nm^{-1}, to directly monitor changes to the intensity of the elastically scattered signal, as well as the intensity and spectral shift of the inelastic signal to fully account for all the scattered photons detected. Another X-ray scattering spectrometer was placed in the backscattering non-collective geometry (k = 52 nm^{-1}) as a relative calibration measurement to normalize the total scattering cross section following the f-sum rules of particle conservation. Both spectrometers used Highly Annealed Pyrolytic Graphite (HAPG) crystals as dispersive elements in Von-Hamos-geometry with Cornell SLAC Pixel Array Detectors (CSPADs). The angularly resolved diagnostic consisted of a large CSPAD used to measure the solid structure *via* the Bragg reflections in order to properly normalize and deconvolve the characteristic changes in the elastic scattering contributions to

the static structure factor. A high-resolution silicon crystal spectrometer in transmission of the X-ray beam was also used to monitor the input spectrum for each individual X-ray pulse.

The ultrabright properties of the LCLS together with a 1 Hz fs-laser and novel H_2 microjet allow for X-ray scattering from materials with a low scattering cross section. High repetition rate data collection can be used for single photon detection whereby accumulating and averaging photon counts over many scattering events can produce a highly precise, background limited data set with large signal-to-noise ratio [30]. The spectrally resolved X-ray Thomson scattering intensity profiles, in **Figure 1**, are shown for the forward and backward scattering geometries along with the measured X-ray diffraction patterns. **Figure 3** demonstrates the reduction in error of the X-ray Thomson signal strength by accumulating scattering events using this experimental platform.

3 X-RAY THOMSON SCATTERING

The total scattered X-ray spectrum demonstrates a unique intensity profile and spectral shape that depends on a combination of scattering contributions that are distinctly related to the temperature, density, and ionization state of the plasma. The total scattered cross section (**Eq. 1**) can be described in terms of σ_T, the Thomson scattering cross-section, the dynamic electron structure factor $S_{ee}^{tot}(k,\omega)$, and k_1 and k_0, the scattered and incident wave vectors, respectively:

$$\frac{d^2\sigma}{d\Omega d\omega} = \sigma_T \frac{k_1}{k_0} S_{ee}^{tot}(k,\omega) \tag{1}$$

Simultaneous high-resolution angularly and spectrally resolved X-ray Thomson scattering (XRTS) has proven to be an accurate method to infer the electron density, temperature, and pressure of dense plasmas [8, 31]. Combining direct measurements of the static structure factor with inelastic scattering by free electrons, and in some cases, bound-free or resonant inelastic scattering transitions [32–35] allow for the ability to accurately calculate the ion temperature, the electron temperature, and the ionization of hydrogen throughout the entire relaxation from a non-equilibrium plasma.

3.1 Quasi-Elastic X-Ray Scattering

It is possible to separate the total density fluctuations included in the electronic structure factor, $S_{ee}^{tot}(k,\omega)$, between three contributing cross sections [36, 37]. These include the free electrons, $Z_f S_{ee}^{0}(k,\omega)$, the bound electrons that are directly photoionized from the X-ray radiation, $Z_b \int \tilde{S}_{ce}(k,\omega-\omega') S_a^S(k,\omega')\, d\omega'$, and from electrons in the system that are bound to and weakly follow the ion motion, $W_R(k)$.

For a partially ionized hydrogen plasma, the total elastic X-ray scattering response is caused by multiple species, described by the following decomposition [38]:

$$W_R(k) = \sum_{a,b} \sqrt{x_a x_b} \left| f_a(k) + q_a(k) \right| \left| f_b(k) + q_b(k) \right| S_{ab}(k), \tag{2}$$

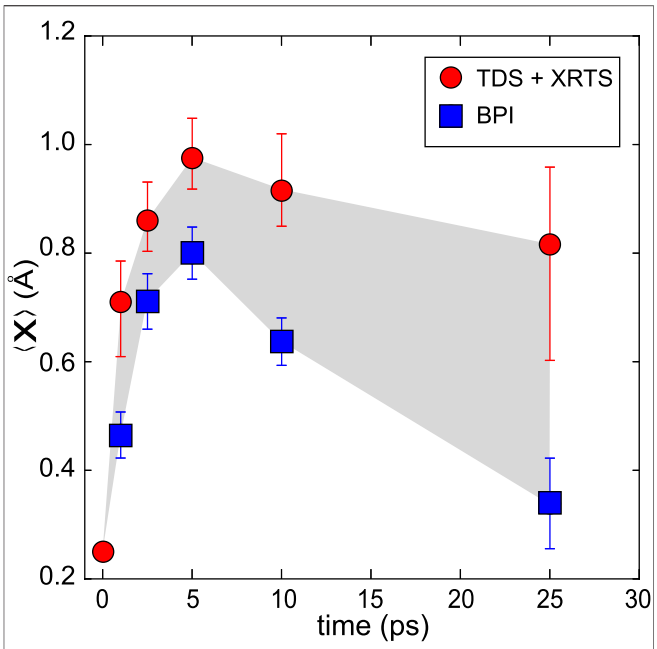

FIGURE 2 | Temporally resolved mean displacement as calculated from the total elastic XRTS signal at W_R (k = 4.8 nm^{-1}) and the average Bragg peak intensity (BPI) measured at 40.5°, 43°, and 46°; (blue circles) thermal diffuse scatter inferred from Bragg peak Intensity; (red circles) combination of XRTS and thermal diffuse scatter (TDS) as measured by the crystal spectrometer. Excess signal indicates total contribution from XRTS.

where $x_i = n_i / \sum_i n_i$ is the concentration of ion species **i**, with n_i its density. Here, $f_a(k)$ are the atomic form factors describing the elastic scattering from bound electrons, $q_a(k)$ contains the contributions from the electrons in the screening clouds around the ions of species a in a partially ionized plasma [35, 39], and $S_{ab}(k)$ are the partial static ion-ion density structure factors [40]; where statistically $S_{ab}(k) = \int S_{ab}(k,\omega) d\omega$ [39].

3.2 Debye-Waller Factor

The Debye-Waller factor $2W = k^2 < u^2 >$ is determined by the mean-square displacements of atoms, $< u^2 >$, which is a result of any departure from the perfectly regular lattice, including both long-range and short-range disorders. The total nearly elastic response with the solid structure factor $S(k, t)$ is understood by $S(k,t) = S_t(k)[1 - e^{-2W} + e^{-2W} b(k)]$ where $S_t(k)$ is defined as the translational structure factor and the diffraction intensity $b(k) = \frac{1}{N} \sum_{r,s}^{n} e^{ik\cdot(U_r - U_s)} \rightarrow 0$ outside of the Bragg peak. The change in the intensities of diffraction peaks, $\frac{I}{I_0} = e^{-2W}$, has been widely used to study lattice melting [41–43] with ultrafast heating, and suppression of lattice distortion [41, 44–46]. The Debye-Waller factor is only related to the long-range disorder and the XRTS is a indication of short-range liquid-like disorder from the plasma, where the latter is dominated by region of interest.

The background contribution is caused by heating of the H_2 solid from hot electrons that propagate transversely to the H_2 jet axis and can dislocate, or heat, the atoms in the lattice. The heating of the solid lattice from hot electrons can cause atomic

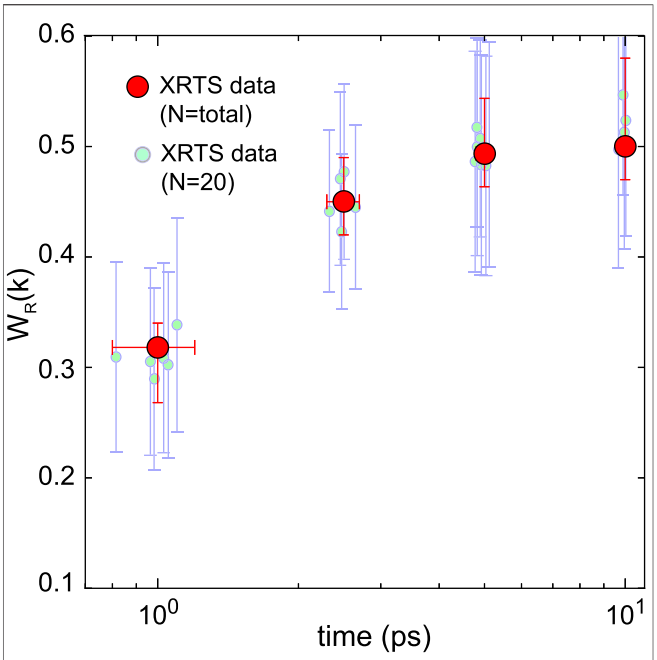

FIGURE 3 | (color online) Time resolved evolution of the elastic XRTS scattering intensity calculated with the average on-target signal that accumulated for N = 20 hits (blue circles) and for the total integrated signal (red circles).

displacements that lead to a diffuse elastic signal increase at low scattering angles according to the Debye-Waller effect [47]. Such a signal has to be accounted for and corrected by applying the Debye-Waller factor to the observed intensity increase. Simultaneously recording angularly resolved measurements of the Bragg peak intensity (BPI) (**Figure 2**), it is possible to decouple the contribution from the thermal diffuse scatter (TDS) with that of the X-ray Thomson scattered signal [48]. Direct measurements of the BPI can be used to account for any excess signal measured at low angles. Any long-range disorder, generated by hot electrons immediately after laser irradiation outside of the focal region, will result in an increase in the TDS and a decrease in the BPI. The excess elastic signal can be quantified and is plotted in **Figure 3**.

3.3 Ion Structure Factors

The ion structure factors account for the correlations between, and densities of, the ion species that make up the plasma. The observed Rayleigh amplitude (**Figure 4**) is a sum of atom-atom (H-H), proton-proton (p-p), and atom-proton (H-p) contributions. These contributions include the dissociation in the system, starting from a diatomic molecular solid and ending as a partially ionized plasma. Due to only short range van der Waals type interactions between the atoms, the atom-atom structure factor remains close to unity for all wavenumbers. Combining this with the form factor of the bound 1s electrons means that the atoms provide a significant, but temperature independent, part of the elastic signal. On the other hand, the screening cloud around the protons, as well as the correlation hole in the proton-proton structure, are intrinsically temperature dependent and contribute to the elastic peak at small wavenumbers in a characteristic way to allow temperature determination. The measured intensity of the this Rayleigh contribution to the XRTS signal (**Figure 3**) demonstrates a clear increase for each measured time step. Such a change is the result of an increasing ion temperature, and additionally contains information about the electron temperature due to the contributions from the electrons in the screening clouds that surround the ions. To fully interpret and constrain the plasma conditions with respect to the ionization, requires wavenumber resolved intensity distributions measured with a fixed angle CSPAD visualized in **Figure 4**.

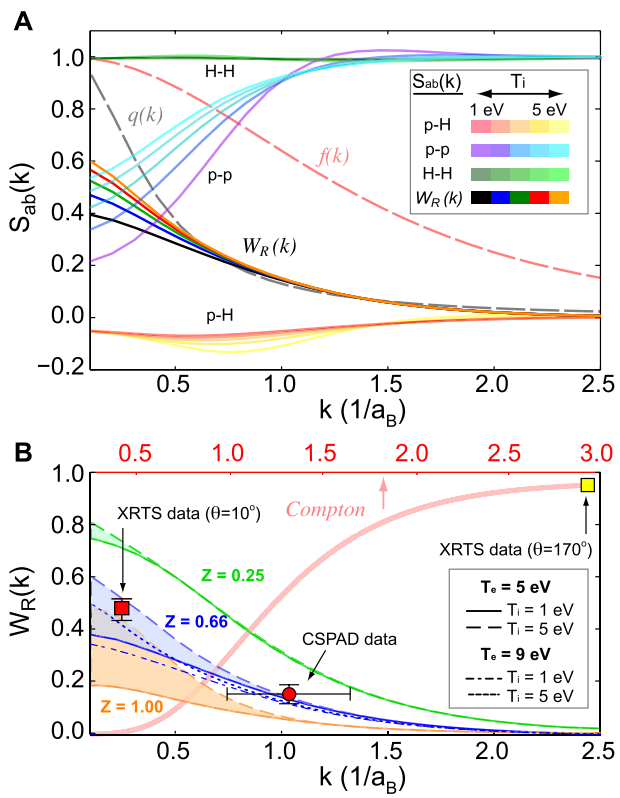

FIGURE 4 | (color online) **(A)** Non-equilibrium HNC static structure factor for hydrogen as a function of ion temperature, at a fixed electron temperature of T_e = 5 eV, showing all contributing correlations ($S_{ab}(k)$) in a partially ionized plasma of Z = 0.66. The hydrogen-hydrogen (black line), proton-proton (blue line), and hydrogen-proton (red line) distributions/structure as well as contributions from the screening cloud q(k) (dashed grey), atomic form factor f(k) (dashed red). **(B)** Quasi-elastic X-ray Thomson scattering data measured for high-q and low-q spectrometers compared to theoretical static structure factors using Z_f = 1.0, Z_f = 0.66, and Z_f = 0.25 measured at t = 2.5 ps? Each ionization includes the angular intensity distribution for T_i = 1 eV and T_i = 5 eV for an electron temperature of T_e = 5 eV and T_e = 9 eV plotted for Z_f = 0.66. The red square data point is a measurement of the background corrected elastic signal strength W_R (k = 52 nm^{-1}) representing a unique combination of T_e and T_i conditions, and the yellow data point is the inelastic Compton signal (k = 4.8 nm^{-1}) used to normalize all signal strength measurements. The red circle data point is the average background corrected intensity signals measured with the CSPAD as a way to benchmark the ionization (Z_f).

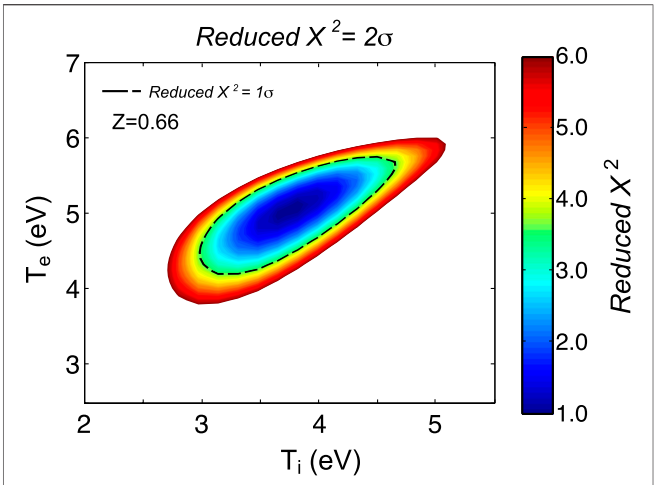

FIGURE 5 | Reduced chi squared contour plot showing the deviations between theoretical fits to the measured XRTS signal strength (excluding the inelastic and thermal diffuse scatter) for various electron and ion temperatures, at time t = 2.5 ps? The plot shows a global minimum at T_e = 5 eV and T_i = 3.8 eV. All possible T_e and T_i conditions within a 2σ deviation are plotted. The black dashed line indicates a measured 1σ deviation.

The unique signal strength measured from the XRTS when combined with the intensity contributions measured on the CSPAD detector can be used to monitor the non-equilibrium dynamics during relaxation from a temperature of T_e = 10 eV and T_i = 1 eV. **Figure 4** shows an example, at time t = 2.5 ps, of how the XRTS signal can be used to infer the ionization, the electron temperature, and the ion temperature of the plasma. Using the relative magnitude of the quasi-elastic signal intensity, it is possible to ascertain Z_f, T_e, and the T_i of the system for each time step in order to resolve the energy relaxation dynamics. Additionally, we can use the derived ionization of Z = 0.66 as a direct comparison to the theoretical dynamic ionization rate equations, Saha calculations using ionization potential depression models for the temperature dependent equilibrium states, and density-functional theory molecular dynamics (DFT-MD) simulations that verify the pair distribution and the electron occupation around the ion [49].

To determine the plasma conditions from the measured XRTS intensity, we apply an analysis with χ^2 statistics over a wide range of electron and ion temperature space for a fixed ionization see **Figure 5**. The optimal conditions are defined by minimizing the mean square deviation between total data intensity and the model intensity, that is χ^2, whereas the quality and robustness is estimated by the values of χ^2 in the electron and ion temperature region around the global minimum. The method of least squares is based on the concept that the optimum description of a set of data is one that minimizes the weighted sum of the squares of the deviation of the data from the theoretically produced values. The weighted sum is minimized (2σ) for an electron temperature between 3.7 and 6.0 eV, for an ion temperature between 2.6 and 5.1 eV using 0.1 eV step sizes. Furthermore the ionization goodness of fit can be tested and minimized for each χ^2 iteration.

4 DTF-MD SIMULATIONS

Microcanonical DFT-MD simulations were performed to model the ion temperature of the heated system for a given electron temperature determined independently with 3D particle in cell (PIC) simulations using the OSIRIS code [49–51]. At an initial temperature of $T_e \sim 10$ eV, it is possible estimate the initial non-thermal crystal mismatch heating of cryogenic molecular hydrogen, see **Figure 6**. For cryogenic hydrogen, we prepared the initial state of the system as an hcp lattice with randomly oriented hydrogen molecules at the lattice positions. The lattice parameters were $a = 4.1\mathring{A}$, $c = 1.64a$ in line with the mass density of fluid cryogenic hydrogen of $\rho = 0.07$ g/cm^3. As can be seen in **Figure 6**, the ion temperature rises to at least ~ 9000 K within tens of femto-seconds after start of the run.

The amount of ionization may be inferred from computation of the ion-ion and ion-electron static structure factors [49]. The generalized screening cloud $\rho(k)$, i.e., the electronic density around an ion, may be deconvolved from the electron-ion structure *via*

$$\rho(k) = \frac{S_{ei}(k)}{S_{ii}(k)} = (1 - Z) \cdot f(k) + Z \cdot q(k), \tag{3}$$

and can then be fitted by the average charge state Z, the atomic form factor of hydrogen $f(k)$, and the screening cloud $q(k)$. From these calculations, the average charge state of $Z = 0.66$ and initial ion temperature of $T_i \sim 1$ eV have been derived and were subsequently used in the analysis of the weight of the Rayleigh peak. Using the charge state of the hydrogen system as determined by DFT-MD, hypernetted chain integral equation (HNC) calculations [49] were performed for a wide variety of electron and ion temperatures to obtain the partial static structure factors as needed for the weight of the Rayleigh peak based on the multi-component Chihara formula [38].

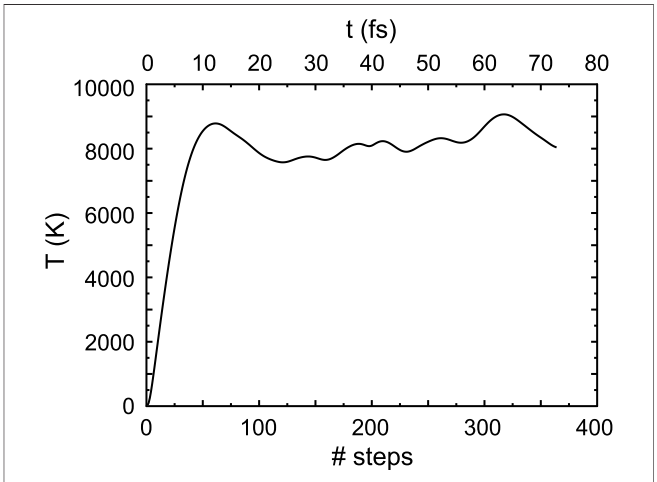

FIGURE 6 | Microcanonical DFT-MD simulation of the first tens of femtoseconds of laser irradiated cryogenic molecular hydrogen. ρ =0.07 g/cm^3, T_e = 10 eV, T_i^0 = 25 K.

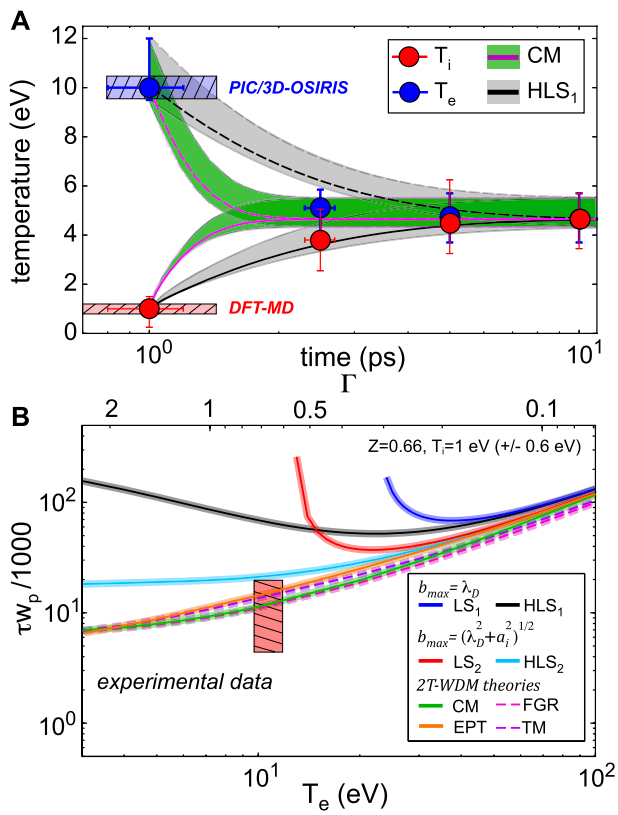

FIGURE 7 | (color online) **(A)** Temporal evolution of the electron temperatures (blue circles) and ion temperatures (red circles) as measured with XRTS. Predictions of the equilibration from various energy relaxation models. The curves are calculated from time t = 1 ps using $n_e = 3 \times 10^{22}$ cm^{-3}, $T_e = 10$ eV, $T_i = 1$ eV, and Z = 0.66 as parameter inputs. Line thickness indicates uncertainty in T_i. **(B)** Experimentally determined relaxation time τ/1,000, in units of the inverse electron-plasma frequency plotted together with eight energy relaxation theories from the warm dense state to the classical conditions. Four classical and quasi-classical theories: Landau-Spitzer (LS) relaxation using different Coulomb logarithms $\Lambda_{LS} = \ln(b_{max}/b_{min})$, hyperbolic Landau-Spitzer (HLS), $\Lambda_{HLS} = \frac{1}{2}\ln(1 + (b_{max}^2/b_{min}^2))$ where $b_{min} = (\lambda^2 + \rho_\perp^2)^{1/2}$ for all cases. Four 2T-WDM theories: coupled mode (CM) [15], Fermi golden rule (FGR) [28], T-matrix (TM) [14], and effective potential theory (EPT) [29].

5 RESULTS

The specific ion temperature condition of $T_i = 1$ eV, measured at t = 1 ps, is consistent with the determined energy release caused by the fs-laser induced ionization of the molecular H-H bond, shown in **Figure 6**. The instantaneous change of the proton-proton potential to a Coulomb potential gives kinetic thermal motion to the ions at sub-ps times before the thermalization is dominated by the electron-ion energy exchange. This has been modeled and verified using ab initio DFT-MD simulations, highlighted by the red shaded region in **Figure 7A**. Additionally the electron temperature has been modeled independently with 3D-PIC OSIRIS simulations, as shown in **Figure 1**, and agrees with the measured conditions shown by the blue shaded region [49] in **Figure 7A**. The time behavior can be compared to analytical predictions after uniform heating is achieved for t > 1 ps? The measured electron and ion temperatures are plotted as a function of time delay in **Figure 7A**. The data is plotted together with two energy transfer models using the charge state Z = 0.66. The different theoretical models use an initial electron temperature as observed from the XRTS measurements at t = 1 ps, where the 9 and 12 eV error bounds stem from the error analysis of the spectrally resolved data. One model uses a Landau-Spitzer like theory (HLS) of relaxation *via* binary collisions, valid in the classical high-temperature region, with a Coulomb logarithm that cannot become negative for high densities [14].

5.1 Two-Temperature Relaxation Rates

A quantitative comparison of the relaxation rates (i.e., the equilibration time from 1 ps) for many widely referenced analytical models with that of the experimentally determined energy transfer rate can be observed in **Figure 7B**. The upper limit of the experimental data region was determined by the overlap probability of the T_e and T_i data points for each time step plotted in **Figure 7A**. The width of the region indicates the uncertainty in T_e. The models tested includes energy transfer *via* Landau-Spitzer rates with different choices for the cut-off parameters in the Coulomb logarithm [14], rates based on Fermi golden rule [28], T-matrix approximation [14], and energy transfer rates *via* collective modes [15, 16] that include a quantum binary collision model incorporating dynamic screening. Additionally the effective potential theory [29, 52], which models binary scattering using the potential of mean force, both agree with the measurements. The EPT calculation in **Figure 7B** applies the classical theory [29], however this can be extended to dense plasmas using the average atom two-component plasma model [53, 54]. A Fermi golden rule [28] or T-matrix approximation [14] would give identical results due to the relatively small temperature difference [15]. Other advanced relaxation models using non-equilibrium molecular dynamics that predict slower energy exchange rates, such as the constrained electron force field (CEFF) method are also in agreement with the experimental results [18]. A direct comparison is not presented here, however the equilibration time for similar conditions is well within the upper error limit of our measurements. As can be seen in **Figure 7B**, all LS-type models using a general or modified Coulomb logarithm results in equilibration times that are too long. Future LCLS studies performed with this diagnostic platform will be able to unequivocally distinguish between the energy exchange rate of these advanced models *via* enhanced signal to noise, or by probing states of hydrogen that are significantly more dense.

6 SUMMARY

Our results show the first experimentally determined relaxation rates from a dense two-temperature plasma in a non-equilibrium state. The findings allow for a quantitative comparison of various analytical models for the electron-ion energy transfer in the warm dense matter regime where many theories are untested. Such theories can be implemented in radiation-hydrodynamic codes to improve equation of state properties that are important for both ICF and self-constricted plasmas produced in Z-pinches. The results are important for understanding heat transport in dense systems where classical plasma theory breaks down and modified or capped substitutions to the Coulomb logarithm are commonly used.

DATA AVAILABILITY STATEMENT

The raw data supporting the conclusions of this article will be made available by the authors, without undue reservation.

AUTHOR CONTRIBUTIONS

Experiment setup and data collection was performed by LF, WS, SG, UZ, BB, ZC, TD, MG, JK, DK, MM, AP, AR, and CR. Facility support and preparation was provided by EG, EG, and HL under the leadership of AF. DFT-MD simulations were performed by JV. PIC and OSARIS simulations were provided by CR, EA, and RM under the leadership of FF. CR, SB, RB, JV, and DG provided energy relaxation theory and calculations. RR and DG provided senior leadership and XRTS analysis supervision. SG supervised all aspects of the data collection, analysis, and manuscript writing. LF wrote the paper with input from all authors.

FUNDING

This work is supported by the DOE Office of Science, Fusion Energy Science under FWP 100182 and FWP 100237. The work was carried out at the MEC end-station of the LCLS. Use of the LCLS, SLAC National Accelerator Laboratory, is supported by the U.S. Department of Energy, Office of Science, Office of Basic Energy Sciences under Contract No. DE-AC02-76SF00515. The MEC instrument has additional support from the DOE Office of Science, Office of Fusion Energy Sciences under contract No. SF00515. The work of TD was performed under the auspices of the U.S. Department of Energy by Lawrence Livermore National Laboratory under Contract No. DE-AC52-07NA27344. FF acknowledges the OSIRIS Consortium, consisting of UCLA and IST (Portugal) for the use of OSIRIS 3.0 framework and visXD framework. The 3D OSIRIS simulations were run on Mira (ALCF supported under Contract No. DE-AC02-06CH1135) through an ALCC award. RR thanks the DFG for support within the SFB 652.

SUPPLEMENTARY MATERIAL

The Supplementary Material for this article can be found online at: https://www.frontiersin.org/articles/10.3389/fphy.2022.838524/full#supplementary-material

REFERENCES

1. Kroupp E, Osin D, Starobinets A, Fisher V, Bernshtam V, Weingarten L, et al. Ion Temperature and Hydrodynamic-Energy Measurements in aZ-Pinch Plasma at Stagnation. *Phys Rev Lett* (2011) 107:105001. doi:10.1103/physrevlett.107.105001
2. Lindl JD, Amendt P, Berger RL, Glendinning SG, Glenzer SH, Haan SW, et al. The Physics Basis for Ignition Using Indirect-Drive Targets on the National Ignition Facility. *Phys Plasmas* (2004) 11:339–491. doi:10.1063/1.1578638
3. Mackinnon AJ, Kline JL, Dixit SN, Glenzer SH, Edwards MJ, Callahan DA, et al. Assembly of High-Areal-Density Deuterium-Tritium Fuel from Indirectly Driven Cryogenic Implosions. *Phys Rev Lett* (2012) 108:215005. doi:10.1103/PhysRevLett.108.215005
4. Glenzer SH, Callahan DA, MacKinnon AJ, Kline JL, Grim G, Alger ET, et al. Cryogenic Thermonuclear Fuel Implosions on the National Ignition Facility a. *Phys Plasmas* (2012) 19:056318.
5. Hammel BA, Haan SW, Clark DS, Edwards MJ, Langer SH, Marinak MM, et al. High-mode Rayleigh-taylor Growth in Nif Ignition Capsules. *High Energy Density Physics* (2010) 6:171–8. doi:10.1016/j.hedp.2009.12.005
6. Glenzer SH, Redmer R X-ray Thomson Scattering in High Energy Density Plasmas. *Rev Mod Phys* (2009) 81:1625–63. doi:10.1103/revmodphys.81.1625
7. García Saiz E, Gregori G, Gericke DO, Vorberger J, Barbrel B, Clarke RJ, et al. Probing Warm Dense Lithium by Inelastic X-ray Scattering. *Nat Phys* (2008) 4:940–4. doi:10.1038/nphys1103
8. Fletcher LB, Lee HJ, Döppner T, Galtier E, Nagler B, Heimann P, et al. Ultrabright X-ray Laser Scattering for Dynamic Warm Dense Matter Physics. *Nat Photon* (2015) 9:274–9. doi:10.1038/nphoton.2015.41
9. Glenzer SH, Fletcher LB, Galtier E, Nagler B, Alonso-Mori R, Barbrel B, et al. Matter under Extreme Conditions Experiments at the Linac Coherent Light Source. *J Phys B: Mol Opt Phys* (2016) 49:092001. doi:10.1088/0953-4075/49/9/092001
10. Sperling P, Gamboa EJ, Lee HJ, Chung HK, Galtier E, Omarbakiyeva Y, et al. Free-electron X-ray Laser Measurements of Collisional-Damped Plasmons in Isochorically Heated Warm Dense Matter. *Phys Rev Lett* (2015) 115:115001. doi:10.1103/physrevlett.115.115001
11. Mabey P, Richardson S, White TG, Fletcher LB, Glenzer SH, Hartley NJ, et al. A strong Diffusive Ion Mode in Dense Ionized Matter Predicted by Langevin Dynamics. *Nat Commun* (2017) 8:14125. doi:10.1038/ncomms14125
12. Fäustlin RR, Bornath T, Döppner T, Düsterer S, Förster E, Fortmann C, et al. Observation of Ultrafast Nonequilibrium Collective Dynamics in Warm Dense Hydrogen. *Phys Rev Lett* (2010) 104:125002.
13. Zastrau U, Sperling P, Harmand M, Becker A, Bornath T, Bredow R, et al. Resolving Ultrafast Heating of Dense Cryogenic Hydrogen. *Phys Rev Lett* (2014) 112:105002. doi:10.1103/physrevlett.112.105002
14. Gericke DO, Murillo MS, Schlanges M. Dense Plasma Temperature Equilibration in the Binary Collision Approximation. *Phys Rev E Stat Nonlin Soft Matter Phys* (2002) 65:036418. doi:10.1103/PhysRevE.65.036418
15. Vorberger J, Gericke DO, Bornath T, Schlanges M. Energy Relaxation in Dense, Strongly Coupled Two-Temperature Plasmas. *Phys Rev E Stat Nonlin Soft Matter Phys* (2010) 81:046404. doi:10.1103/PhysRevE.81.046404
16. Dharma-Wardana MWC, Perrot F Energy Relaxation and the Quasiequation of State of a Dense Two-Temperature Nonequilibrium Plasma. *Phys Rev E* (1998) 58:3705–18. doi:10.1103/physreve.58.3705
17. Benedict LX, Surh MP, Stanton LG, Scullard CR, Correa AA, Castor JI, et al. Molecular Dynamics Studies of Electron-Ion Temperature Equilibration in Hydrogen Plasmas within the Coupled-Mode Regime. *Phys Rev E* (2017) 95:043202. doi:10.1103/PhysRevE.95.043202
18. Ma Q, Dai J, Kang D, Murillo MS, Hou Y, Zhao Z, et al. Extremely Low Electron-Ion Temperature Relaxation Rates in Warm Dense Hydrogen: Interplay between Quantum Electrons and Coupled Ions. *Phys Rev Lett* (2019) 122:015001. doi:10.1103/PhysRevLett.122.015001
19. Landau LD. Kinetic Equation for the Coulomb Effect. *Physikalische Z der Sowjetunion* (1936) 10:154.
20. Spitzer L. *Physics of Fully Ionized Gases*. Chelmsford, MA, USA: Courier Corporation (2006).
21. Hansen JP, McDonald IR Thermal Relaxation in a Strongly Coupled Two-Temperature Plasma. *Phys Lett A* (1983) 97:42–4. doi:10.1016/0375-9601(83)90097-x
22. Reimann U, Toepffer C Collision Times in Plasmas. *Laser Part Beams* (1990) 8:763–70. doi:10.1017/s0263034600009150
23. Li C-K, Petrasso RD Fokker-planck Equation for Moderately Coupled Plasmas. *Phys Rev Lett* (1993) 70:3063–6. doi:10.1103/physrevlett.70.3063

24. Lee YT, More RM An Electron Conductivity Model for Dense Plasmas. *Phys Fluids* (1984) 27:1273–86. doi:10.1063/1.864744
25. Celliers P, Ng A, Xu G, Forsman A Thermal Equilibration in a Shock Wave. *Phys Rev Lett* (1992) 68:2305–8. doi:10.1103/physrevlett.68.2305
26. Ng A, Celliers P, Xu G, Forsman A Electron-ion Equilibration in a Strongly Coupled Plasma. *Phys Rev E* (1995) 52:4299–310. doi:10.1103/physreve.52.4299
27. Riley D, Woolsey NC, McSherry D, Weaver I, Djaoui A, Nardi E X-ray Diffraction from a Dense Plasma. *Phys Rev Lett* (2000) 84:1704–7. doi:10.1103/physrevlett.84.1704
28. Vorberger J, Gericke DO Coupled Mode Effects on Energy Transfer in Weakly Coupled, Two-Temperature Plasmas. *Phys Plasmas* (2009) 16:082702. doi:10.1063/1.3197136
29. Baalrud SD, Daligault J Effective Potential Theory for Transport Coefficients across Coupling Regimes. *Phys Rev Lett* (2013) 110:235001. doi:10.1103/physrevlett.110.235001
30. Fletcher LB, Zastrau U, Galtier E, Gamboa EJ, Goede S, Schumaker W, et al. High Resolution X-ray thomson Scattering Measurements from Cryogenic Hydrogen Jets Using the Linac Coherent Light Source. *Rev Sci Instrum* (2016) 87:11E524. doi:10.1063/1.4959792
31. Ma T, Döppner T, Falcone RW, Fletcher L, Fortmann C, Gericke DO, et al. X-ray Scattering Measurements of strong Ion-Ion Correlations in Shock-Compressed Aluminum. *Phys Rev Lett* (2013) 110:065001. doi:10.1103/PhysRevLett.110.065001
32. Glenzer SH, Landen OL, Neumayer P, Lee RW, Widmann K, Pollaine SW, et al. Observations of Plasmons in Warm Dense Matter. *Phys Rev Lett* (2007) 98:065002. doi:10.1103/PhysRevLett.98.065002
33. Lee HJ, Neumayer P, Castor J, Döppner T, Falcone RW, Fortmann C, et al. X-ray thomson-scattering Measurements of Density and Temperature in Shock-Compressed Beryllium. *Phys Rev Lett* (2009) 102:115001. doi:10.1103/physrevlett.102.115001
34. Fletcher LB, Kritcher AL, Pak A, Ma T, Döppner T, Fortmann C, et al. Observations of Continuum Depression in Warm Dense Matter with X-ray thomson Scattering. *Phys Rev Lett* (2014) 112:145004. doi:10.1103/physrevlett.112.145004
35. Chapman DA, Vorberger J, Fletcher LB, Baggott RA, Divol L, Döppner T, et al. Observation of Finite-Wavelength Screening in High-Energy-Density Matter. *Nat Commun* (2015) 6:6839. doi:10.1038/ncomms7839
36. Chihara J Difference in X-ray Scattering between Metallic and Non-metallic Liquids Due to Conduction Electrons. *J Phys F: Met Phys* (1987) 17:295–304. doi:10.1088/0305-4608/17/2/002
37. Chihara J Interaction of Photons with Plasmas and Liquid Metals - Photoabsorption and Scattering. *J Phys Condens Matter* (2000) 12:231–47. doi:10.1088/0953-8984/12/3/303
38. Wünsch K, Vorberger J, Gregori G, Gericke DO. X-ray Scattering as a Probe for Warm Dense Mixtures and High-Pressure Miscibility. *Europhysics Lett* (2011) 94:25001.
39. Gericke DO, Vorberger J, Wünsch K, Gregori G. Screening of Ionic Cores in Partially Ionized Plasmas within Linear Response. *Phys Rev E Stat Nonlin Soft Matter Phys* (2010) 81:065401. doi:10.1103/PhysRevE.81.065401
40. Gericke DO, Murillo MS, Semkat D, Bonitz M, Kremp D Relaxation of Strongly Coupled Coulomb Systems after Rapid Changes of the Interaction Potential. *J Phys A: Math Gen* (2003) 36:6087–93. doi:10.1088/0305-4470/36/22/334
41. Siders CW, Cavalleri A, Sokolowski-Tinten K, To´th C, Guo T, Kammler M, et al. Detection of Nonthermal Melting by Ultrafast X-ray Diffraction. *Science* (1999) 286:1340–2. doi:10.1126/science.286.5443.1340
42. Siwick BJ, Dwyer JR, Jordan RE, Miller RJD An Atomic-Level View of Melting Using Femtosecond Electron Diffraction. *Science* (2003) 302:1382–5. doi:10.1126/science.1090052
43. Mo MZ, Chen Z, Li RK, Dunning M, Witte BBL, Baldwin JK, et al. Heterogeneous to Homogeneous Melting Transition Visualized with Ultrafast Electron Diffraction. *Science* (2018) 360:1451–5. doi:10.1126/science.aar2058
44. Zhu P, Cao J, Zhu Y, Geck J, Hidaka Y, Pjerov S, et al. Dynamic Separation of Electron Excitation and Lattice Heating during the Photoinduced Melting of the Periodic Lattice Distortion in 2h-Tase2. *Appl Phys Lett* (2013) 103:071914. doi:10.1063/1.4818460
45. Gao M, Lu C, Jean-Ruel H, Liu LC, Marx A, Onda K, et al. Mapping Molecular Motions Leading to Charge Delocalization with Ultrabright Electrons. *Nature* (2013) 496:343–6. doi:10.1038/nature12044
46. Eichberger M, Schäfer H, Krumova M, Beyer M, Demsar J, Berger H, et al. Snapshots of Cooperative Atomic Motions in the Optical Suppression of Charge Density Waves. *Nature* (2010) 468:799–802. doi:10.1038/nature09539
47. Warren BE. *X-ray Diffraction*. Chelmsford, MA, USA: Courier Corporation (1969).
48. Gregori G, Glenzer SH, Landen OL. Generalized X-ray Scattering Cross Section from Nonequilibrium Plasmas. *Phys Rev E Stat Nonlin Soft Matter Phys* (2006) 74:026402. doi:10.1103/PhysRevE.74.026402
49. [Dataset]. See supplemental materials (-).
50. Fonseca RA, Silva LO, Tsung FS, Decyk VK, Lu W, Ren C, et al. Osiris: a Three-Dimensional, Fully Relativistic Particle in Cell Code for Modeling Plasma Based Accelerators. In: International Conference on Computational Science. Berlin, Germany: Springer (2002). p. 342–51. doi:10.1007/3-540-47789-6_36
51. Fonseca RA, Martins SF, Silva LO, Tonge JW, Tsung FS, Mori WB One-to-one Direct Modeling of Experiments and Astrophysical Scenarios: Pushing the Envelope on Kinetic Plasma Simulations. *Plasma Phys Control Fusion* (2008) 50:124034. doi:10.1088/0741-3335/50/12/124034
52. Baalrud SD Transport Coefficients in Strongly Coupled Plasmas. *Phys Plasmas* (2012) 19:030701. doi:10.1063/1.3690093
53. Daligault J, Baalrud SD, Starrett CE, Saumon D, Sjostrom T Ionic Transport Coefficients of Dense Plasmas without Molecular Dynamics. *Phys Rev Lett* (2016) 116:075002. doi:10.1103/PhysRevLett.116.075002
54. Starrett CE, Saumon D Electronic and Ionic Structures of Warm and Hot Dense Matter. *Phys Rev E Stat Nonlin Soft Matter Phys* (2013) 87:013104. doi:10.1103/PhysRevE.87.013104

Conflict of Interest: The authors declare that the research was conducted in the absence of any commercial or financial relationships that could be construed as a potential conflict of interest.